

# Chapter 1

## Supplementary Theory

### 1.1 Quantum Charge Transport

One of main discussions of this work is the effect of quantum charge transport on plasmon coupling. Both quantum tunnelling and ballistic transport are qualitatively described in the main text for simplicity. The following section shows the relevant mathematical derivations of the simplest cases of quantum tunnelling and ballistic transport.

#### 1.1.1 Quantum Electron Tunnelling

#### 1.1.2 Ballistic Conduction

A 1D constriction between two charge reservoirs of length  $L$  and width  $W$  can be described as either diffusive if  $l, l_\phi \ll L, W$ , ballistic if  $l, l_\phi \gg L, W$ , or quasi-ballistic if inbetween, where  $l$  and  $l_\phi$  are the mean free path and phase coherence length, respectively. Conductance in the diffusive regime is as classically expected,  $G = \sigma_{2D}W/L$ . In the ballistic regime, however, it inherits quantum properties as is thus given by the Landauer formula,

$$G = \frac{2e^2}{h}T(E_F), \quad (1.1)$$

where  $T(E_F)$  is the transmission coefficient of an electron at the Fermi level. This is derived from the current flowing through a barrier between two biased reservoirs, whereby the Fermi levels are related via  $E_{F,L} - E_{F,R} = eV$ . The leftwards current through a barrier is given by,

$$I_L = 2e \int_0^\infty f(E(k), E_{F,L})v(k)T(k)\frac{dk}{2\pi}, \quad (1.2)$$

where  $f(E, E_F)$  is the Fermi-Dirac function and the wavevector of an electron can be related to its energy via  $dE = \hbar v dk$ . Converting Eq. 1.2 to an energy basis and adding the rightwards

current yields,

$$I_L = \frac{2e}{h} \int_{E_L}^{\infty} [f(E(k), E_{F,L}) - f(E(k), E_{F,R})] T(E) dE. \quad (1.3)$$

In the small bias limit<sup>1</sup> the Fermi-Dirac function is expanded as a Taylor series into,

$$f(E(k), E_{F,L}) - f(E(k), E_{F,R}) \approx eV \frac{\delta f(E(k), E_F)}{\delta E_F}. \quad (1.4)$$

Substituting this into Eq. 1.3 yields the integral,

$$I_L = \frac{2e^2 V}{h} \int_{E_L}^{\infty} \left[ -\frac{\delta f}{\delta E} \right] T(E) dE. \quad (1.5)$$

At low temperatures  $\delta f/\delta E \rightarrow \delta(E - E_F)$  and the integral evaluates to,

$$I_L = \frac{2e^2 V}{h} T(E_F), \quad (1.6)$$

from which the conductance  $G = I/V$  is derived to be,

$$G = \frac{2e^2}{h} T(E_F). \quad (1.7)$$

With the barrier still in place this corresponds to a tunnelling conductance with  $T(E_F) < 1$ . The point at which the barrier disappears ( $E_{barrier} = E_F$ ) gives rise to  $T(E) = 1$  and opens up a single quantised conductance channel. Adding additional  $n$  sub-bands into the constriction continues to increase the conductance by its quantum,  $2e^2/h$ , and thus the conductance of a 1D *conductive* junction can be expressed as,

$$G = \frac{2e^2}{h} n. \quad (1.8)$$

---

<sup>1</sup>Large biases are ignored

# Chapter 2

## Supplementary Experimental Details

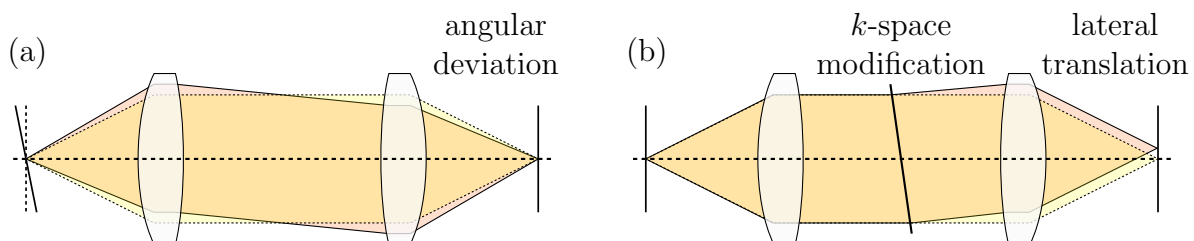
### 2.1 Supplementary Optical Details

Features, design justifications and optics theory not essential to the main text are detailed here. The following paragraphs clarify the advantages of the reimaging technique, the limitations in choice of objective lens, beamsplitters and optical bench layout. Lastly, further useful information and optics characterisation, such as the range of laser powers, are presented.

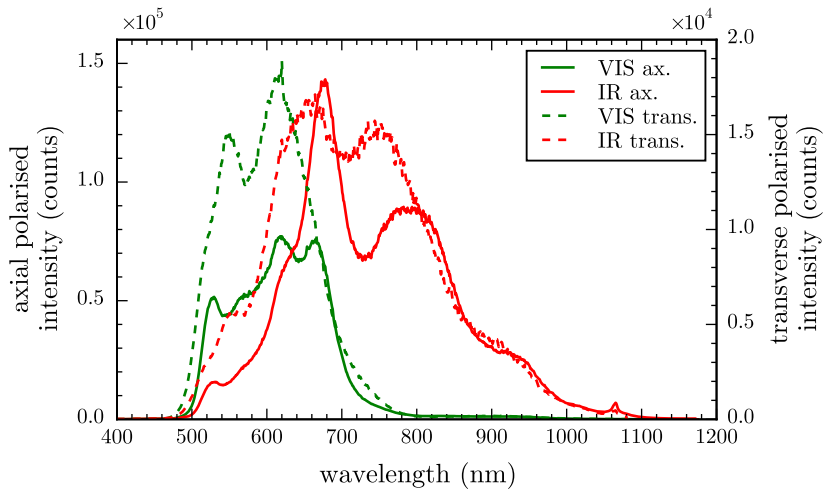
#### 2.1.1 Optical Design

The concept of reimaging, and its effect on beam alignment, is shown in Figure ???. The ray diagrams show that the beam position in the focus can be adjusted by changing the angle of a mirror placed in the Fourier plane (in the case of the microscope the mirror directly after the DF stop). The shape of the beam, dictated by its angular distribution in Fourier space, is controlled by tilting a mirror in a focal plane (the mirror in the focus of the reimaging arm). The two mirrors provide independent control over the two main beam properties.

The choice of objective was determined by the overall range over which a reference spectrum from a Ag mirror is valid. Two long working distance objectives suitable for single

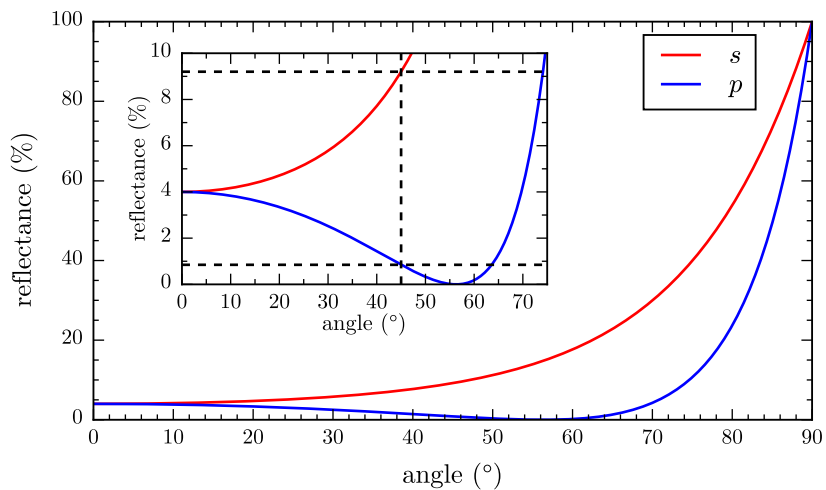


**Concept of reimaging for beam alignment.** Adjusting the angle of the beam in a focal plane does not change the position of the focus in the image (front focal) plane but changes the position in the Fourier (back focal) plane. Adjusting the angle of the beam in a Fourier plane translates the position of the beam in the image plane without changing its angular components.

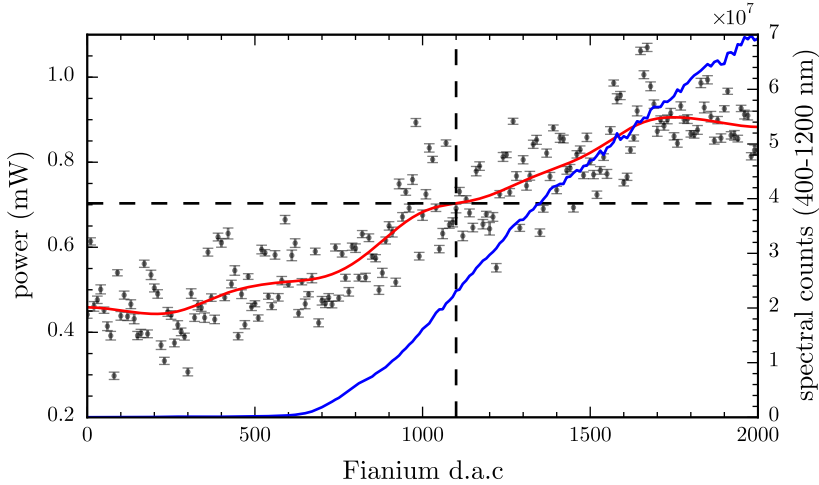


**Spectral comparison between VIS and IR objectives.** The VIS objective is an Olympus 100 $\times$  0.9 NA MPlan BD dark-field objective whereas the IR objective is an Olympus 100 $\times$  0.8 NA MPlan bright-field objective.

nanostructure spectroscopy were characterised for use in the microscope: a VIS and a IR objective. The raw spectra measured using each of the objectives is shown in Figure ???. The sharp cut-on at 480 nm is due to the supercontinuum laser. The VIS objective clearly outperforms the IR objective below 625 nm, though both objective counts are large enough to maintain a good reference signal. Overall, references using the VIS objective only extend marginally more below 500 nm. However, the sharp 700 nm cut-off in the VIS objective means that it is not suitable for spectra in the NIR. The reference signal of the VIS objective is only valid up until 900 nm whereas the IR objective extends to 1100 nm. The gain in spectral range means that the IR objective is chosen despite its lack of dark-field illumination for imaging.



**Reflectance as a function of angle of incidence for glass-air interface.** Reflective is calculated from the fresnel coefficients. The refractive index of glass is assumed to be  $n = 1.5$ . The inset shows a zoomed segment in the low reflectance regime.



**Fianium power incident on the back aperture of the objective as a function of driving current.** The beam diameter is restricted to the size of the back aperture to accurately measure the power throughput without measuring extra power not transmitted to the sample plane. Error bars represent the precision (standard error) of 1000 repeat measurements at each power, hence they are small, however the large distribution of points shows that the power meter is only accurate to 1 mW.

Consideration was given when designing the optical layout to account for intensity differences in each linear polarisation. Reflection and transmission of an incident EM wave at an interface between two refractive media is characterised by the Fresnel equations, with reflectance given by,

$$R_s = \left| \frac{n_1 \cos \theta_i - n_2 \cos \theta_t}{n_1 \cos \theta_i + n_2 \cos \theta_t} \right|^2, \quad (2.1)$$

$$R_p = \left| \frac{n_1 \cos \theta_t - n_2 \cos \theta_i}{n_1 \cos \theta_t + n_2 \cos \theta_i} \right|^2, \quad (2.2)$$

where the wave impinges on the interface at an angle  $\theta_i$  and refracts into a transmitted angle  $\theta_t$  due to the refractive index change from  $n_1$  to  $n_2$ . The angles are related using  $n_2 \sin \theta_t = n_1 \sin \theta_i$ . As shown in Figure ??, there is a large difference in reflectance between linear polarisations at higher angles of incidence. The microscope is designed such that the *s*-polarisation corresponds to light polarised along the tip axis, maximising its transmission to the spectrometers.

### 2.1.2 Optical Characterisation

The measured broadband power incident on the back aperture of the objective (removing the contribution from over-filling of the back aperture using an iris) is shown in Figure ???. The power is measured using a thermopile bolometer (Coherent Powermax) with simultaneous measurements of the spectral counts of the *s*-polarised signal component summed between

400–1200 nm. The supercontinuum laser is driven with a d.a.c. of 1100 in most experiments. Under these conditions, less than 1 mW is used to illuminate samples, enough that reflection from a reference substrate just under saturates the spectrometer counts. Assuming a spot size on  $\mathcal{O}(1 \mu\text{m})$  means a focal intensity of  $10^8 \text{ mW cm}^{-2}$ . Sub-mW powers are sufficient to maintain good signals without risking damage to nanoscale samples.

## 2.2 Supplementary Electronics

The circuitry of the microscope electronics is shown in Figure 2.1.

## 2.3 Software Lock-In Derivation

To lock into only the signal component at the reference frequency  $\omega_r$  a reference wave needs to be computed. The first step in the lock-in process is to mathematically construct a single frequency waveform at the correct harmonic using the supplied reference signal. The reference signal is typically of the form  $A \sin(\omega_{rs}t + \phi_r)$ , but the algorithm will also work with any periodic function since it triggers off a rising position edge. When  $\sin(\theta) = 0$  and the gradient is positive ( $\cos(\theta) = 1$ )  $\theta = 2n\pi$ . Hence the rising edge trigger points  $t_i$  occur at,

$$\theta = \omega_{rs}t_i + \phi_r = 2n\pi. \quad (2.3)$$

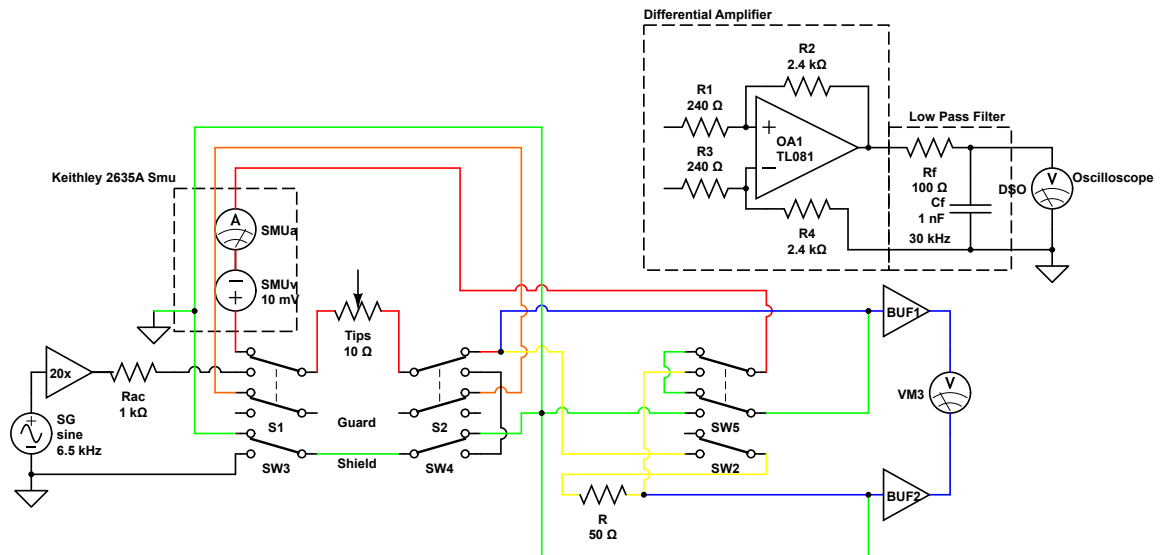


**Figure 2.1: Schematic of the electrical measurement circuit.** The central routing box allows switching between a.c. and d.c. circuits and low-and high-bandwidth d.c. measurements. The a.c. circuit is used to align two AFM probes together while the d.c. circuit is used to measure spatially dependent signals from the gap between two AFM probes.

Trigger times are fitted against the number of triggers (number of periods) since the start of the signal using,

$$t_i = \frac{1}{\omega_{rs}}(2n\pi - \phi_r) = \frac{2\pi}{\omega_{rs}}n - \frac{\phi_r}{\omega_{rs}}. \quad (2.4)$$

A complex reference wave of the form  $e^{ih(\omega_{rs}t+\phi_r)}$ , where  $h$  is the harmonic of the reference frequency  $\omega_{rs}$  required to lock into the frequency  $\omega_r$ , is constructed from the  $t_i = mn + c$  fit using,

$$\omega_{rs} = \frac{2\pi}{m}, \quad (2.5)$$

$$\phi_r = \frac{mc}{2\pi}. \quad (2.6)$$

The frequency component of the signal at  $\omega_r = h\omega_{rs}$  can be extracted using Fourier analysis,

$$Z_s(\omega_r) = \frac{2}{t} \int_0^t Z_s(t)e^{-ih(\omega_{rs}t+\phi_r)} dt. \quad (2.7)$$

Discretising this not a programmable form results in,

$$Z_s(\omega_r) = \frac{2}{n} \sum_0^n Z_s(t_n)e^{-ih(\omega_{rs}t_n+\phi_r)} \quad (2.8)$$

where  $\text{Re}[Z_s(\omega_r)]$  and  $\text{Im}[Z_s(\omega_r)]$  are the  $x$  and  $y$  of the signal component at  $\omega_r$ , respectively. Polar coordinates of amplitude and phase are retrieved using the coordinate transforms,

$$r = \sqrt{x^2 + y^2}, \quad (2.9)$$

$$\phi = \tan^{-1}(y/x). \quad (2.10)$$

## 2.4 Capacitive Alignment Model Derivation

Beginning with the general equation of motion for two cantilevers, denoted by  $i = (1, 2)$ , with initial positions  $z_{0i}$ , spring constants  $k_{0i}^z$ , masses  $m_i$ , damping coefficients  $\beta_i^z$ , and resonant frequencies  $\omega_{0i} = \sqrt{k_{0i}/m_i}$ , separated by a distance  $d(t) = z_1(t) - z_2(t)$  and coupled via the  $z$ -components of the long range attractive electrostatic driving force  $F_{EL}^z$  and short range ( $\mathcal{O}(\text{nm})$ ) Van der Waals and repulsive tip-tip interaction forces  $F_{TT}^z$ . The equilibrium separation between tips is denoted by  $d_0 = z_{01} - z_{02}$ . The equation of motion in the  $z$ -axis of the two parallel cantilevers of spring constant  $k_i^z = k_{0i}^z + k_{TT}^z$  and damping coefficient  $\beta_i^z = \beta_{0i}^z + \beta_{TT}^z$  is given by,

$$m_i \frac{d^2 z_i}{dt^2} + \beta_i^z \frac{dz_i}{dt} + k_i^z (z_i - z_{0i}) = \pm (F_{EL}^z + F_{TT}^z), \quad (2.11)$$

where the sign of the force depends on the tip - positive for one tip and negative for the other. Tip-tip interactions can be ignored and  $F_{TT}^z = 0$  by assuming alignment takes place at long range and therefore  $\beta_{TT}^z = k_{TT}^z = 0$ . Further assume that one cantilever remains stationary. The apex separation is then restricted to  $d = z_1$  with an equilibrium separation  $d_0 = z_{01}$ . Under these conditions the motion reduces to that of a single tip,

$$m_1 \frac{d^2 z_1}{dt^2} + \beta_1^z \frac{dz_1}{dt} + k_1^z (z_1 - z_{01}) = F_{EL}^z(z_1, t). \quad (2.12)$$

The substitution  $z_r = z_1 - z_{01} = d - d_0$  can simplify the equation to using a single relative variable,

$$m_1 \frac{d^2 z_r}{dt^2} + \beta_1^z \frac{dz_r}{dt} + k_1^z z_r = F_{EL}^z(z_r, t), \quad (2.13)$$

This equation now describes the whole system rather than each individual tip with the main reference point between tips being the equilibrium separation  $d_0$ .

The remaining force exerted between tips is purely electrostatic and depends on voltage  $V$  and capacitance  $C$ . In general an electrostatic force acting in one direction can be calculated using,

$$F^z(V, z) = \frac{\partial U(V, z)}{\partial z}, \quad (2.14)$$

where the electrostatic potential is given by,

$$U(V, z) = \frac{C(z)V^2}{2}. \quad (2.15)$$

The force is then given by,

$$F_{EL}^z(V, z) = \frac{1}{2} \frac{\partial C(z)}{\partial z} V^2(t), \quad (2.16)$$

where  $C(z)$  is the capacitance between the cantilevers when separated by a distance  $d = z_1 - z_2$  and  $V(t)$  is the potential difference. Under the parallel plate capacitor model the capacitance is,

$$C(z) = \frac{\varepsilon_0 A_{ov}}{z_1} + C_{bk}, \quad (2.17)$$

for plates with  $A_{ov}$  area of overlap, including a stray capacitance  $C_{bk}$ . Applying a harmonic driving force at a frequency  $\omega_s$ ,

$$V(t) = V_0 \cos(\omega_s t), \quad (2.18)$$

results in a nonlinear driving force, given by,

$$F_{EL}^z(z_1, t) = \frac{-\varepsilon_0 A_{ov} V(t)^2}{4z_1^2}. \quad (2.19)$$

The square of a harmonic signal doubles the frequency as per,

$$V(t)^2 = V_0^2 \cos^2(\omega_s t) = \frac{V_0^2}{2} [1 + \cos(2\omega_s t)], \quad (2.20)$$

hence the driving force becomes,

$$F_{EL}^z(z_1, t) = \left( \frac{-\varepsilon_0 A_{ov} V_0^2}{4z_1^2} \right) [1 + \cos(\omega_p t)], \quad (2.21)$$

where  $\omega_p = 2\omega_s$  is the cantilever pump frequency.

Substituting Eq. 2.21 into Eq. 2.12 gives the simplified equation of motion for the dual-tip system,

$$m_1 \frac{d^2 z_1}{dt^2} + \beta_{01}^z \frac{dz_1}{dt} + k_{01}^z (z_1 - d_0) = \left( \frac{-\varepsilon_0 A_{ov} V_0^2}{4z_1^2} \right) [1 + \cos(\omega_p t)]. \quad (2.22)$$

Driving at a pump frequency close to the cantilever resonance ( $\omega_p \approx \omega_{01}$ ) therefore leads to strong resonant oscillations between tips.

Expressing Eq. 2.22 in terms of  $z_r$  and  $d_0$  yields,

$$m_1 \frac{d^2 z_r}{dt^2} + \beta_{01}^z \frac{dz_r}{dt} + k_{01}^z z_r = \left( \frac{-\varepsilon_0 A_{ov} V_0^2}{4(z_r + d_0)^2} \right) [1 + \cos(\omega_p t)], \quad (2.23)$$

and enables further simplification via approximation. Assuming that  $z_r \ll d_0$  the right hand side of Eq. 2.23 can be taken to first order using a Taylor series,<sup>1</sup>

$$m_1 \frac{d^2 z_r}{dt^2} + \beta_{01}^z \frac{dz_r}{dt} + k_{e1}^z z_r \simeq \left( \frac{-\varepsilon_0 A_{ov} V_0^2}{4d_0^2} \right) [1 + \cos(\omega_p t)], \quad (2.24)$$

where,

$$k_{e1}^z = k_{01}^z - \left( \frac{\varepsilon_0 A_{ov} V_0^2}{2d_0^3} \right) [1 + \cos(\omega_p t)]. \quad (2.25)$$

This effective spring constant  $k_{e1}^z$  does not cause parametric mixing as it oscillates at  $\omega_p$  and so its effect can be averaged out over time resulting in  $\langle k_{e1}^z \rangle = k_{01}^z - \varepsilon_0 A_{ov} V_0^2 / 2d_0^3$ . Defining the constant  $q$  as,

$$q = \left( \frac{-\varepsilon_0 A_{ov} V_0^2}{4d_0^3} \right), \quad (2.26)$$

the effective spring constant can be expressed as,

$$k_{e1}^z = k_{01}^z + 2q [1 + \cos(\omega_p t)], \quad (2.27)$$

$$\langle k_{e1}^z \rangle = k_{01}^z + 2q, \quad (2.28)$$

---

<sup>1</sup> $F(z_r) = F(0) + \left. \frac{dF(z_r)}{dz_r} \right|_0 z_r = \left( \frac{-\varepsilon_0 A_{ov} V_0^2}{4} \right) [1 + \cos(\omega_p t)] \left( \frac{1}{d_0^2} - \frac{2z_r}{d_0^3} \right)$

and the EOM can be again rewritten in the form,

$$m_1 \ddot{z}_r + \beta_{01}^z \dot{z}_r + [\langle k_{e1}^z \rangle + 2q \cos(\omega_p t)] z_r - q [1 + \cos(\omega_p t)] d_0 \simeq 0, \quad (2.29)$$

Equation Eq. 2.29 is of the form of the driven damped Mathieu equation,

$$\ddot{z} + 2\kappa \dot{z} + [a - 2q \cos(2t)] z = 0, \quad (2.30)$$

and has solutions in the limit of small oscillations of,

$$z_1 \approx d_0 - |z_1^{off}| - z_{m1} \cos(\omega_p t + \varphi_1) \quad (2.31)$$

where

$$z_1^{off} \approx \frac{\varepsilon_0 A_{ov} V_0^2}{4d_0^2 \langle k_{e1}^z \rangle}, \quad (2.32a)$$

$$z_{m1} \approx \frac{\varepsilon_0 A_{ov} V_0^2}{4d_0^2 \sqrt{(\langle k_{e1}^z \rangle - m_1 \omega_p^2)^2 + (\beta_{01}^z \omega_p)^2}}, \quad (2.32b)$$

$$\varphi_1 \approx \tan^{-1} \left( \frac{\beta_{01}^z \omega_p}{\langle k_{e1}^z \rangle - m_1 \omega_p^2} \right). \quad (2.32c)$$

When extending this to determine current flow, the general current through the tip junction is given by,

$$I(t) = \frac{dQ}{dt} = \frac{d(CV)}{dt} = C(t) \frac{dV(t)}{dt} + V(t) \frac{dC(t)}{dt}. \quad (2.33)$$

Substituting for  $C(t)$  and  $V(t)$  and taking the first few terms in the Taylor series results in the first-order current flow,

$$I(\omega_s) \approx \omega_s C_0 V_0 \left( 1 + \frac{|z_{off}|}{d_0} + \frac{z_{m1}}{2d_0} e^{i\varphi_1} + \frac{C_{bk}}{C_0} \right) e^{i\frac{\pi}{2}}, \quad (2.34a)$$

$$I(\omega_p + \omega_s) \approx \frac{(\omega_p + \omega_s) C_0 V_0 z_{m1}}{2d_0} e^{i(\varphi_1 + \frac{\pi}{2})}, \quad (2.34b)$$

where  $C_0 = \varepsilon_0 A_{ov}/d_0$  and  $z_{off}$  is an additional offset due to  $F_{EL}^z \propto V^2$ .

# Chapter 3

## Fast Spectroscopy of Plasmonic Dimer Make/Break Junctions

One of the aspects of the microscope platform not discussed in the main text is the capability for fast spectroscopy with 10  $\mu\text{s}$  resolution. This was developed in order to measure the initial contact dynamics of plasmonic tip dimers as they come into conductive contact, along with the plasmonics of break junctions formed between the two Au surfaces in a touching tip dimer. Mechanically controllable break junctions (MCBJs) similar to the Au contact formed between tips are well documented and have formed the basis of quantised conductance studies in 3D systems at room temperature (as opposed to the original 2DEG systems) [1–11].

### 3.1 Experimental Setup

The experimental setup for fast spectroscopy is shown in Figure 3.1. Collimated scattered light from the tips is focussed down onto the end of the shutter blade and then, with the shutter open, reimaged onto the entrance slit of a monochromator (Horiba Yvon Jobin Triax 320). The monochromator is paired with a CCD supporting a kinetics readout mode (Princeton Instruments PIXIS 256E), wherein charge is shuffled down the active CCD area after the single top-most line of pixels is exposed to produce a time-series of spectra. The shuffle speed is fast compared with the readout time meaning it is possible to obtain resolutions around 10  $\mu\text{s}$  with the complete image readout only once the kinetics process has completed. Kinetics acquisition is therefore good for measuring short-lived, single-shot events, similar in application to a streak camera. A coarse, 150 lines  $\text{mm}^{-1}$  diffraction grating is chosen to disperse the visible spectrum along the top row of the CCD. The fast spectroscopy path from its initial split off point at the beamsplitter is completely tubed to reduce any background noise incident on the sensitive CCD, with an opening only to place the shutter in the beam.

The kinetics sequence is armed at the start of each experiment, waiting for a trigger

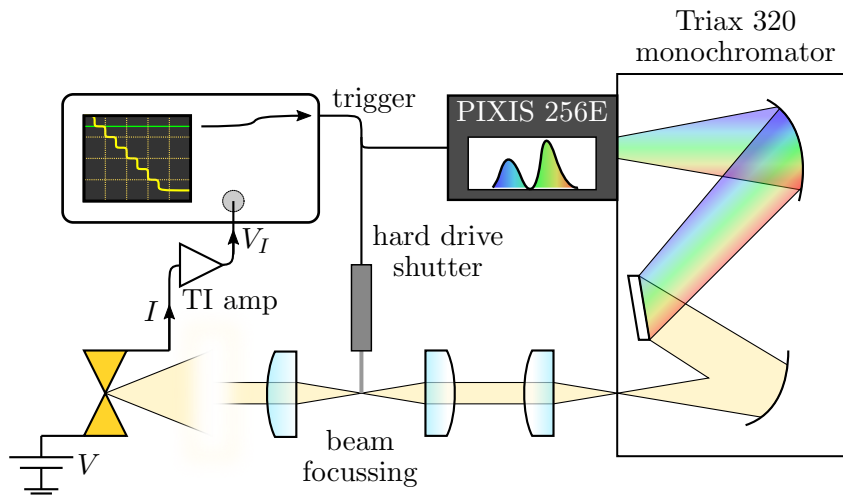


**Figure 3.1: Diagram of the fast spectroscopy setup.** The setup consists of a custom shutter, built from a disassembled hard drive, and a monochromator-CCD pair. Kinetics acquisition on the CCD, along with the shutter mechanism, is triggered by fast electrical signals from the tips which are measured on the oscilloscope.

signal to begin acquisition. To improve the activation time upon receiving the trigger signal non-essential CCD procedures, such as continuous cleaning, are deactivated. The CCD is protected from pre-sequence overexposure by a custom-built fast shutter, constructed using the read head from a disassembled 3.5" computer hard-drive, shown in Figure 3.3. The hard drive is mounted onto a 3D translation stage and the shutter blade is aligned in the focus of the scattered light such that the time taken to uncover the beam is minimised. Regular shutters are limited to 8 ms opening times due to solenoid delay and thus the majority of a short,  $\sim$ 10 ms make/break junction event would be missed. Use of the hard-drive voice coil mechanism enables shutter open times of around 300  $\mu$ s, as confirmed using both CCD and

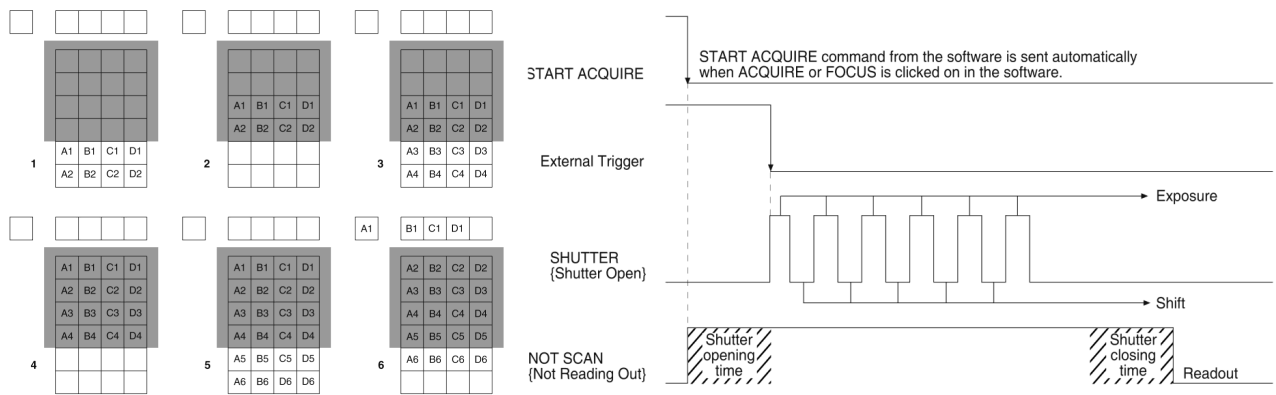


**Figure 3.2: Diagram showing kinetics mode acquisition on the CCD.** An exposed region of the CCD is shuffled into a mechanically or optically masked region. Once the whole CCD has been exposed the image is read out. This acquisition process, along with the opening of the fast shutter, is triggered by an external TTL pulse from an oscilloscope. These images are taken from the Princeton Instruments PIXIS CCD manual.

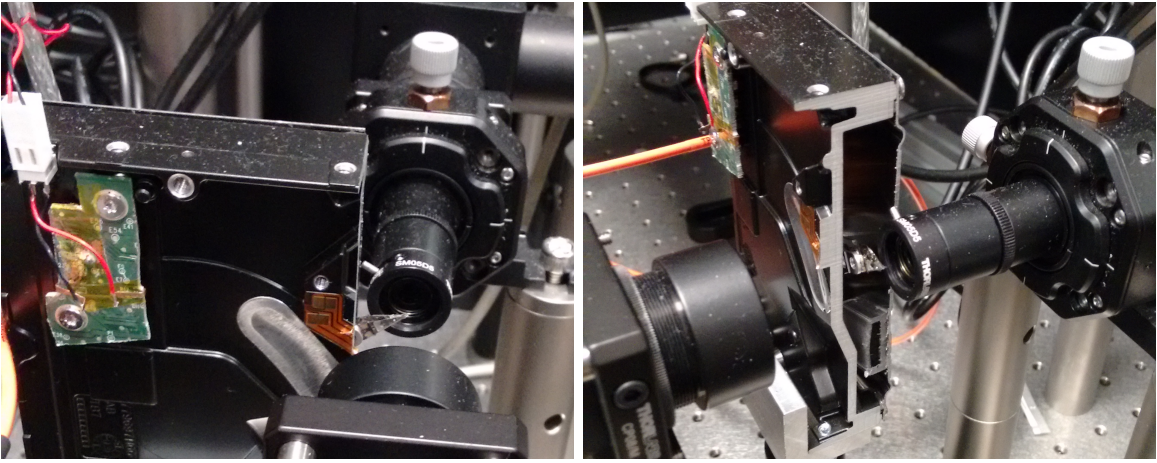


**Figure 3.3: Images of the hard drive shutter.** The shutter works by passing a current through the hard drive voice coil, generating a magnetic field which quickly moves the read head via a Lorentz force. This functions as a shutter blade. The shutter blade is placed in the focus between two lenses in order to uncover the focussed beam spot in the shortest possible time. Rise times in this configuration are around 300  $\mu$ s.

photodiode measurements. Currents to the voice coil and their trigger mechanism are provided by an Arduino microcontroller with a motor driver circuit, enabling up to 2 A of current. The fast trigger mechanism is enabled by directly addressing each bit of the circuit and bypassing the standard Arduino functions. These kinds of shutters have been previously developed [12, 13] though not before with the simplicity of using Arduino circuit boards and programming.

The trigger signal to the CCD and shutter is provided by the oscilloscope. The oscilloscope is set to trigger once the tip junction conductance either rises above  $1G_0$  or falls below  $10G_0$ . As tips come into contact or as the contact area between pulled tips is reduced the number of conductance channels discretely changes by  $G_0$ . The trigger signal synchronises the electronic and spectral measurements to facilitate correlation comparisons. The current limiting resistor described in chapter ?? was installed primarily to prevent the amplifiers feeding the oscilloscope from overloading, thus causing the break junction event to be missed in the time taken for the amplifiers to reset. To ensure correct triggering and optimum electronic measurements, electrical signals passing through the amplified d.c. circuit are cleaned up using low pass filters and a multi-stage (transimpedance) amplification process to maintain a 1 MHz bandwidth at a total gain between  $10^4$ – $10^5$ .

## 3.2 Performance and Issues in Tip Dimer Scanning Experiments

Both make and break contact events typically last no more than 10 ms in the current system, often occurring more on a 100  $\mu$ s–1 ms time scale. The kinetics mode has a minimum acqui-

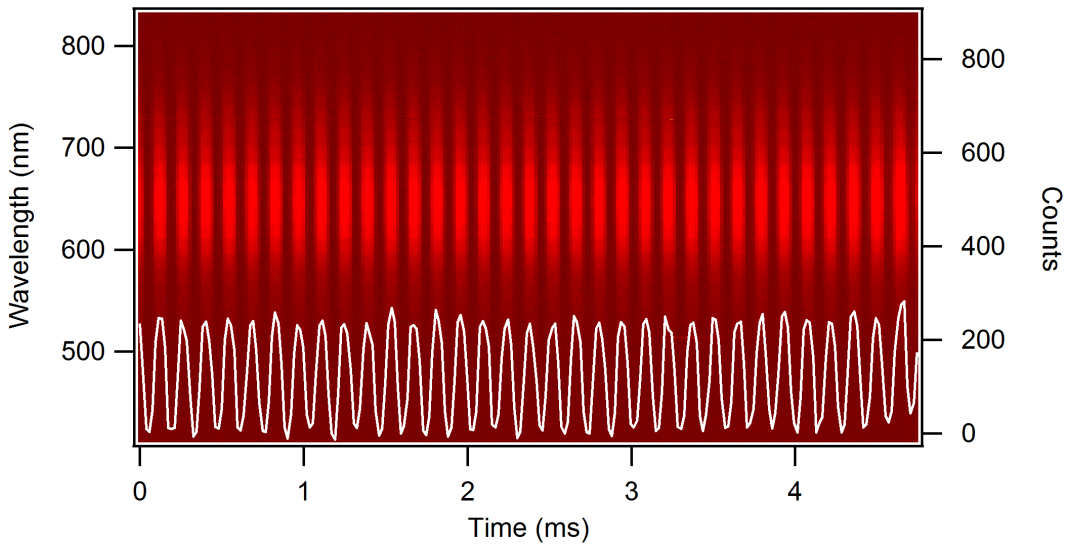


**Figure 3.4: Testing of kinetics mode acquisition.** A reflected supercontinuum beam is chopped and measured both with kinetics mode on the CCD and by a photodiode on the oscilloscope. Oscillations in the beam at the chopping frequency are clearly seen in both the spectral image and the superimposed photodiode output over a 5 ms time period.

sition time of 2.56 ms with a maximum 10  $\mu$ s single spectrum time resolution set by the pixel shift time. The system is trialled using a reflected supercontinuum laser beam with an additional 10  $\mu$ s exposure per row of pixels to give a 5 ms measurement, shown in Figure 3.4. The beam is chopped and measured on a photodiode to show the system is working as expected. Similar tests were performed with an electronically modulated diode laser to determine the time resolution of measurements.

Figure 3.5 shows an example of a conductance traced measured on a break junction between two tips. The traces shows that as the tip contact breaks, the conductance drops in units of  $G_0$ . Under these circumstances the CTP modes sustained by the tip dimer are expected to undergo a redshift with decreasing conductance (ideally in discrete quantised steps). Make junctions, as opposed to break junctions, showed more success in tips since the jump into contact is generally a single high quality event whereas in break junctions the forces holding the tip together and the flexibility of the cantilevers causes issues. Tips often exhibit multiple breaks or changes in conductance as the junction vibrates with the final break occurring only once the gap adhesion forces are overcome. Given the strength of the average tip adhesion (and that it often causes the ball to break from the tip apex) the large amount of pulling force applied to the cantilever leads to a very quick sub- $\mu$ s break event. This is not possible to measure in the given system. Although the make contact event is typically higher quality it is far more difficult to trigger due to operating near the noise floor, often meaning that the  $1G_0$  level is too low to reliably observe.

Though the fast spectroscopy system was engaged in every scan the method provided no

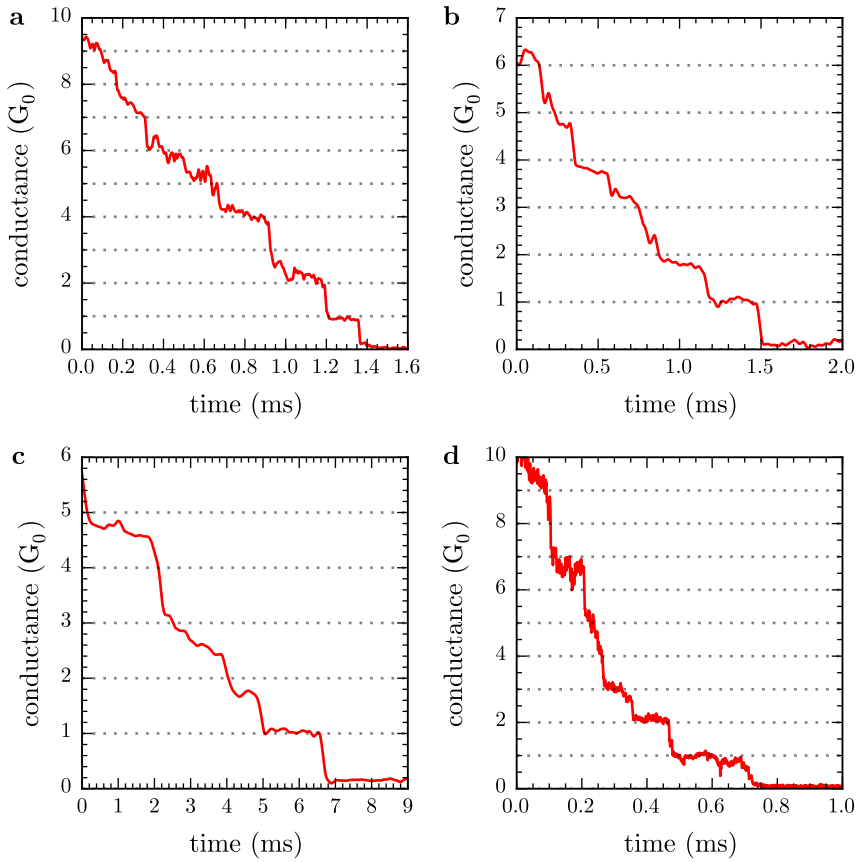


**Figure 3.5: Examples of fast conductance measurements on tip dimer break junctions.** During the break the contact conductance drops in units of  $G_0$  until the last atom-atom contact breaks and tips separate.

useable results. Spectral images contained no detectable signals, as shown in Figure 3.6, due to the short exposure times and low supercontinuum laser powers used to prevent damage to tips. Eventually the  $G_0$ -level conductance data was measured using a slow, controlled make junction in a standard spatial scan (shown in ??b). For this technique to become useful the length of the break or make contact event needs to be lengthened in order to increase the exposure time per row of pixels on the CCD. This could be achieved through more control of the tip position, i.e. by using stiff tips in a low humidity environment to minimise adhesion and more controllably break the contact without significantly bending the cantilever. Alternatively, the increased robustness of the electrochemically fabricated plasmonic tips means increased focal intensities could be sustained. By leveraging both of these suggestions in the future, plasmonic MCBJs could be realised as a means of studying conductance at optical frequencies.

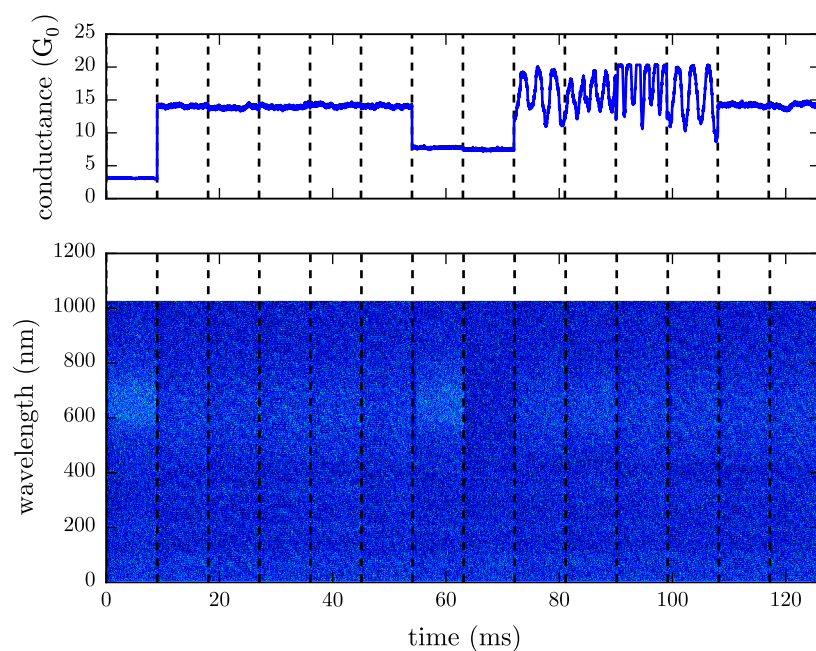


**Figure 3.6:** A representative fast scanning measurement from a plasmonic tip dimer. No signal is detectable with such small exposures per spectrum at acceptable power levels.

# Supplementary References

- [1] J. N. Armstrong et al., Physical Review B **82**, 195416 (2010).
- [2] J. Costa-Krämer et al., Physical Review B **55**, 5416 (1997).
- [3] J. Costa-Krämer, N Garcia, and H. Olin, Physical Review B **55**, 12910 (1997).
- [4] J. Costa-Krämer, Physical Review B **55**, R4875 (1997).
- [5] U. Landman et al., Physical review letters **77**, 1362 (1996).
- [6] D. Natelson, ACS nano **6**, 2871–2876 (2012).
- [7] V. Rodrigues, T. Fuhrer, and D. Ugarte, Physical review letters **85**, 4124 (2000).
- [8] V Rodrigues et al., Physical Review B **65**, 153402 (2002).
- [9] C Sabater et al., arXiv preprint arXiv:1205.4612 (2012).
- [10] M. R. Sørensen, M. Brandbyge, and K. W. Jacobsen, Physical Review B **57**, 3283 (1998).
- [11] I. Yanson et al., Physical review letters **95**, 256806 (2005).
- [12] L. Maguire, S Szilagyi, and R. Scholten, Review of Scientific Instruments **75**, 3077 (2004).
- [13] R. Scholten, Review of scientific instruments **78**, 026101 (2007).